

Metal–Organic-Framework-Derived Carbon Nanostructures for Site-Specific Dual-Modality Photothermal/Photodynamic Thrombus Therapy

Fengrong Zhang, Yuehong Liu, Jiani Lei, Shunhao Wang, Xunming Ji, Huiyu Liu,* and Qi Yang*

Although near-infrared (NIR)-light-mediated photothermal thrombolysis has been investigated to overcome the bleeding risk of clinical clot-busting agents, the secondary embolism of post-phototherapy fragments ($>10\ \mu\text{m}$) for small vessels should not be ignored in this process. In this study, dual-modality photothermal/photodynamic thrombolysis is explored using targeting nanoagents with an emphasis on improving biosafety as well as ameliorating the thrombolytic effect. The nanoagents can actively target glycoprotein IIb/IIIa receptors on thrombus to initiate site-specific thrombolysis by hyperthermia and reactive oxygen species under NIR laser irradiation. In comparison to single photothermal thrombolysis, an 87.9% higher re-establishment rate of dual-modality photothermal/photodynamic thrombolysis by one-time treatment is achieved in a lower limb thrombosis model. The dual-modality thrombolysis can also avoid re-embolization after breaking fibrin into tiny fragments. All the results show that this strategy is a safe and validated protocol for thrombolysis, which fits the clinical translational trend of nanomedicine.

Thrombus associated diseases, such as ischemic stroke, acute myocardial infarction, and deep vein thrombosis, remain the leading causes of death or disability worldwide.^[1] Current clot-busting agents with fibrinolytic drugs as the representatives are widely used in the clinic.^[2] However, the subsequent life-threatening bleeding risk with complicated physical monitoring represents a significant clinical limitation in this treatment.^[3]

Near-infrared (NIR)-light-mediated nano-medicines provide a new therapeutic strategy for thrombus therapy via rapidly converting optical energy into hyperthermia by Landau damping effect.^[4] In 2016, Dash and co-workers first demonstrated that NIR-irradiated gold nanorods possessed antithrombotic properties for dissolving fibrin clots.^[5] After that, van Hest et al. reported a photothermal thrombolytic system based on Janus-type erythrocyte membrane-coated micromotors.^[6] These studies proved that photothermal therapy (PTT) could serve as an effective therapy for thrombolysis with specific spatiotemporal selectivity and minimal invasiveness.^[7] However, PTT might cause severe complications because the small blood vessels are possibly embolized by photothermal thrombolysis fragments, which are usually larger than $10\ \mu\text{m}$. Therefore, a more safe and effective therapy is intensely demanded.


Currently, reactive oxygen species (ROS)-mediated photodynamic therapy (PDT) has been explored for peptide damages of fibrin biopolymers, e.g., polypeptide linkages, noncovalent interactions, and N-attached biantennary glycan region, under the assistance of photosensitizers (PSs).^[8] Therefore, PDT might break the fibrin skeleton of blood clots and prevent secondary embolism from post-photothermal fragments. However, most organic PSs molecules are still limited because of their lack of specific accumulation, poor resistance to photobleaching, and a short half-life period in vivo.^[9] To minimize undesired effects and prevent secondary embolism, we thus hypothesized that an inorganic-nanomaterial-mediated dual-modality photothermal/photodynamic strategy might present superior biosafety as well as thrombolytic effects.

Herein, we developed an Arg-Gly-Asp (RGD)-modified mesoporous carbon nanospheres containing porphyrin-like

F. Zhang, Y. Liu, Prof. Q. Yang
Department of Radiology
Xuanwu Hospital
Beijing 100053, P. R. China
E-mail: yangqi@xwh.ccmu.edu.cn, yangyangqiqi@gmail.com

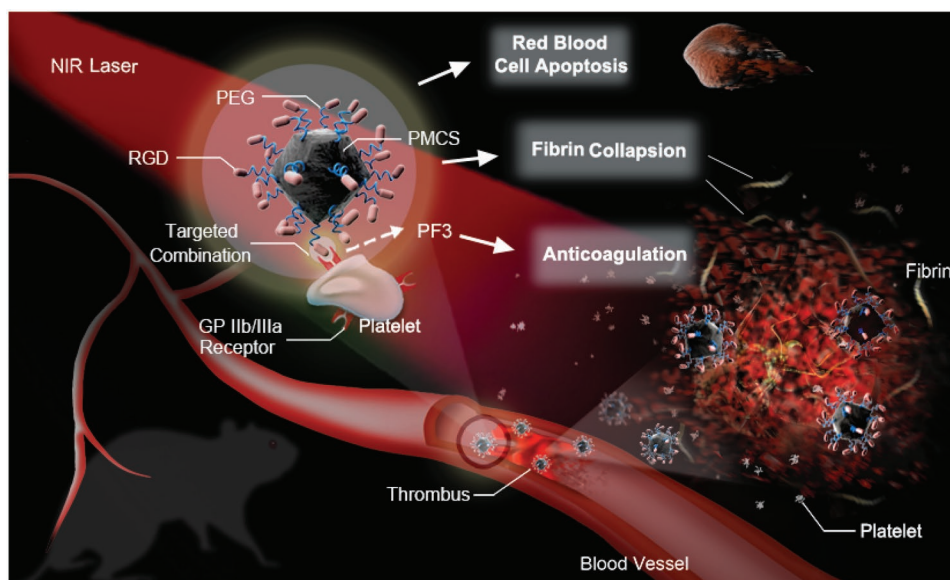
F. Zhang, J. Lei, S. Wang, Prof. H. Liu
Beijing Advanced Innovation Center for Soft Matter Science and Engineering
State Key Laboratory of Organic-Inorganic Composites
Bionanomaterials & Translational Engineering Laboratory
Beijing Key Laboratory of Bioprocess
Beijing Laboratory of Biomedical Materials
Beijing University of Chemical Technology
Beijing 100029, P. R. China
E-mail: liuhy@mail.buct.edu.cn

Prof. X. Ji
Department of Neurosurgery
Xuanwu Hospital
Beijing 100053, P. R. China

 The ORCID identification number(s) for the author(s) of this article can be found under <https://doi.org/10.1002/advs.201901378>.

© 2019 The Authors. Published by WILEY-VCH Verlag GmbH & Co. KGaA, Weinheim. This is an open access article under the terms of the Creative Commons Attribution License, which permits use, distribution and reproduction in any medium, provided the original work is properly cited.

DOI: 10.1002/advs.201901378



Scheme 1. Schematic illustration of RGD-PMCS-mediated site-specific photothermal/photodynamic thrombus therapy.

metal centers (RGD-PMCS), which can initiate the site-specific thrombolysis by hyperthermia and ROS under NIR laser irradiation. The therapeutic mechanism of phototherapy presented in **Scheme 1** provides the following advantages: i) RGD-PMCS could actively target the glycoprotein (GP) IIb/IIIa receptors on activated platelet surfaces,^[10] avoiding the high bleeding risk of the systematic fibrinolytic therapy.^[11] ii) ROS generated by RGD-PMCS could damage the platelet factor 3 (PF3), a kind of lecithin, through lipid peroxidation and inhibit the thrombus recurrence.^[12] iii) The combination of photodynamic and photothermal therapy could greatly increase the efficiency of thrombus breaking and prevent the secondary embolism of larger fragments. On account of these features, this dual-modality PTT/PDT provides a rapid, safe, and effective method for thrombolysis.

Monodisperse metal-organic framework (MOF)-derived mesoporous carbon nanospheres containing porphyrin-like metal centers (PMCS) were synthesized by carbonization of an imidazolate framework based on our previous reports (**Figure 1a**).^[13] The obtained nanostructures were further modified with Vitamin E-poly(ethylene glycol)-COOH (VE-PEG-COOH), then conjugated the RGD motifs via the formation of amide bonds. As shown in **Figure 1b**, the transmission electron microscopy (TEM) image revealed the PMCS with an overall size of about 120 nm. In addition, the hydrodynamic sizes of PMCS and RGD-PMCS revealed by dynamic light scattering (DLS) were 220 and 295 nm, respectively (**Figure 1c**). The negative zeta potential of RGD-PMCS is beneficial to increase the inter-nanoparticles electrostatic repulsion, avoiding capillaries clogging (**Figure 1d**).^[14] Fourier transform infrared spectroscopy was adopted to characterize the chemical composition of PMCS as well as RGD-PMCS and the existence of RGD motifs (**Figure S1**, Supporting Information). The $-\text{CH}_2-$ asymmetric and symmetric stretching vibration of RGD-PMCS had double bands at 2852 and 2928 cm^{-1} , and the characteristic peak (1628 cm^{-1}) was attributed to the stretching vibration of

$\text{C}=\text{O}$. In addition, the peak at 3190 cm^{-1} reflected $-\text{NH}_2$ groups, demonstrating the existence of RGD peptides. Element mapping and energy-dispersive X-ray spectroscopy (EDS) spectra of PMCS and RGD-PMCS indicated that carbon, oxygen, nitrogen, and zinc were homogeneously distributed in the nanoparticles (**Figures S2,S3**, Supporting Information).

NIR region absorption is indispensable for subsequent dual-modality PTT/PDT. The ultraviolet-visible-NIR (UV-vis-NIR) absorption spectrum for PMCS clearly indicated absorption across the spectral range from 300 to 1000 nm, revealing the crucial potential for NIR-mediated phototherapy (**Figure S4**, Supporting Information). And the elevated temperature of PMCS aqueous dispersions with NIR laser irradiation showed the significant concentration- and time-dependency (**Figure 1e**, and **Figure S5a**, Supporting Information). For the PMCS under NIR light irradiation, when the concentration reached up to 100 $\mu\text{g mL}^{-1}$, the temperature boosted to 61.1 $^{\circ}\text{C}$ within 20 min. Furthermore, the photothermal conversion efficiency (η) of PMCS was determined to be 33.3% and the extinction coefficient was calculated to be 6.35 $\text{L g}^{-1} \text{cm}^{-1}$, which was higher than that of many other reported photothermal nanomaterials (**Figure S5b**, Supporting Information).^[15] The high-resolution X-ray photoelectron spectroscopy (XPS) for N1s chemical states were conducted, three remarkable peaks at 398.2, 399.9, and 401.4 eV were assigned to pyridinic, pyrrolic, and graphitic N, respectively (**Figure 1f**). The special zinc-centered porphyrin (a kind of photosensitizer)-like structure in PMCS and the similar coordination number to porphyrin Zn suggested PMCS contains catalytic centers to generate ROS.^[13b] To further explore the intrinsic photodynamic characteristics of PMCS, we measured the singlet oxygen ($^1\text{O}_2$, a kind of ROS) produced by PMCS under NIR laser irradiation with electron spin resonance (ESR) spectroscopy. Compared with other groups, the signal intensity of $^1\text{O}_2$ generated by PMCS with 808 nm laser irradiation showed an approximate onefold increase (**Figure 1g**). These results implied that PMCS had excellent photosensitivity, which

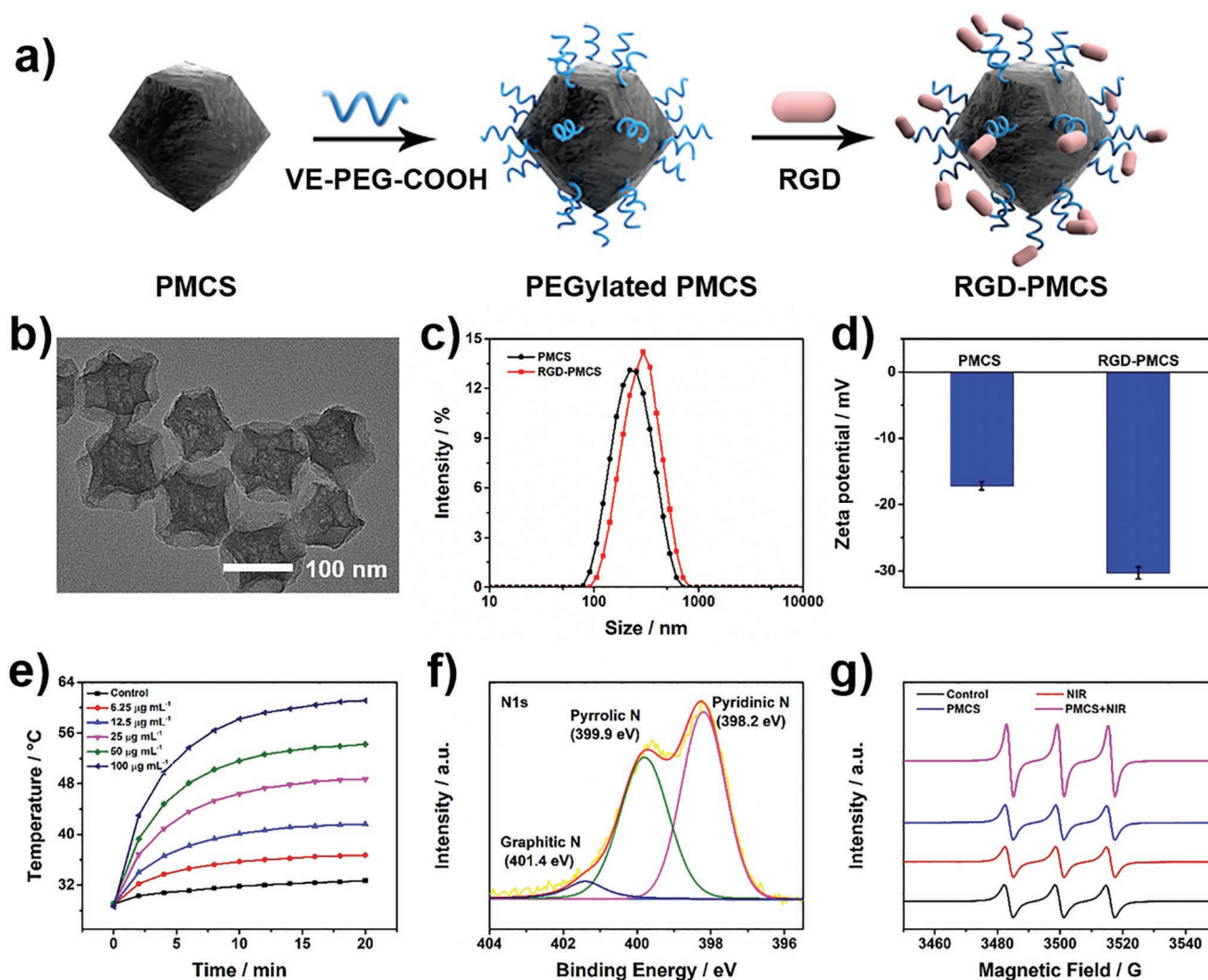


Figure 1. Characterization of PMCS and RGD-PMCS. a) Scheme for RGD-PMCS synthesis. b) TEM image of PMCS. c) Size distribution and d) zeta potentials of PMCS and RGD-PMCS. e) Temperature elevation of PMCS with different concentrations (0, 6.25, 12.5, 25, 50, and 100 $\mu\text{g mL}^{-1}$) under 808 nm laser irradiation (2 W cm^{-2} , 20 min). f) N1s XPS spectra for PMCS. g) ESR spectra of $^1\text{O}_2$ by PMCS (100 $\mu\text{g mL}^{-1}$) with or without NIR laser irradiation (808 nm, 2 W cm^{-2} , 3 min).

provided enormous potential in PTT and PDT for thrombus treatment.

It is well known that activated platelets contact with the subendothelial extracellular matrix at the site of endothelial damage, allowing platelets aggregate and bind to the fibrinogen in plasma with high affinity, causing the formation of thrombus.^[16] Therefore, as shown in **Figure 2a**, platelets were assessed by flow cytometry with the assistance of fluorescein isothiocyanate-CD41 (FITC-CD41) for predicting whether the PSs would trigger platelets activation. Platelets activated with adenosine diphosphate (ADP) were adopted as a positive control.^[17] Conversely, platelets without any treatment were explored as a negative control. Based on the results after co-culturing resting platelets with RGD-PMCS or irradiating by NIR laser, there was nearly no change in comparison with the negative control. In addition, the potential cytotoxicity of PMCS and RGD-PMCS were assessed via measuring human umbilical

vein endothelial cells (HUVEC) viability after co-culturing for 24 h. There was nearly no significant apoptosis or necrosis was observed when the concentration of PMCS and RGD-PMCS ranged from 6.25 to 100 $\mu\text{g mL}^{-1}$ (**Figure 2b**). The hemolysis rate of RGD-PMCS with a series of concentrations was much lower than the upper limited value (5%), confirming excellent biosafety of RGD-PMCS (**Figure 2c**).

Next, to investigate the therapeutic mechanism of the generated ROS by NIR laser irradiation combined with RGD-PMCS, the photodynamic effect of RGD-PMCS + NIR was explored. As indicated in **Figure 2d**, the generation of ROS was detected by 2,7-dichlorodihydrofluorescein diacetate probe. Notably, nearly no fluorescence could be discerned in RGD-PMCS-treated erythrocytes. By comparison, the significant fluorescence signal was presented after exposing to the NIR laser due to the large production of ROS. Then, we further quantitatively analyzed and proved that the production of ROS increased with nanoparticles

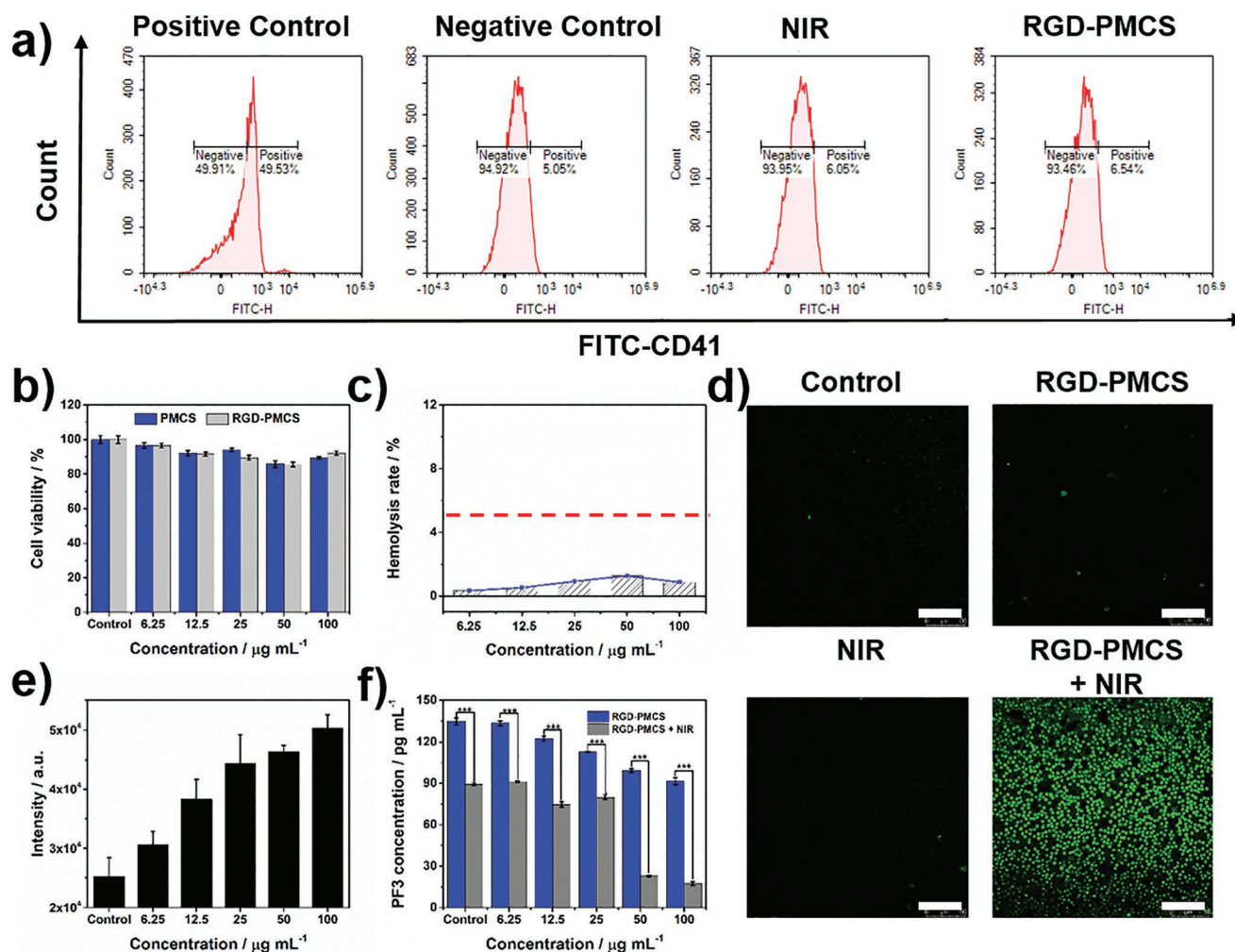


Figure 2. a) Flow cytometry quantification platelets after co-culturing with RGD-PMCS ($100 \mu\text{g mL}^{-1}$) or irradiating by NIR laser (808 nm , 2 W cm^{-2} , 3 min). ADP activated platelets were adopted as positive group. Platelets without any treatment were explored as negative control. b) Relative viabilities of HUVEC after co-incubation with different concentrations of PMCS or RGD-PMCS. c) Hemolysis rate of RGD-PMCS. d) The intracellular ROS production of erythrocytes co-incubated with RGD-PMCS at $100 \mu\text{g mL}^{-1}$ under NIR laser irradiation (808 nm , 2 W cm^{-2} , 3 min). Scale bar = $100 \mu\text{m}$. e) Quantitative analysis ROS generation in erythrocytes after treating with various concentrations of RGD-PMCS combined 808 nm light (2 W cm^{-2} , 3 min). f) Level of PF3 after various treatments. $P > 0.05$, $*P < 0.05$, $**P < 0.01$, $***P < 0.001$.

concentration-dependency, (Figure 2e). Moreover, accumulated studies have indicated that excessive ROS could produce significant lipid peroxidation on phospholipids in cells.^[18] Thus, we hypothesized that ROS induced by RGD-PMCS under NIR laser irradiation could damage PF3. As expected, after exposing to an 808 nm laser, the amount of PF3 dramatically decreased with the increase of RGD-PMCS concentration. Furthermore, RGD-PMCS solution at $100 \mu\text{g mL}^{-1}$ induced about 82.5% PF3 impair, which could provide potential anticoagulant therapy to inhibit re-embolism of blood vessels (Figure 2f).

Encouraged by the satisfactory photothermal and photodynamic performances of RGD-PMCS under NIR laser irradiation, we further conducted an FITC-labeled fibrin clots assay, an intuitive approach for assessing the structural fission of the fibrin skeleton. Importantly, opposed to the green-fluorescence-labeled fibrin without any treatment, the large amount of the collapsed skeleton and small pieces were presented after co-culturing fibrin with RGD-PMCS and exposing with NIR laser,

which indicated that the fiber skeleton was broken by the action of thermal energy and oxidation of ROS (Figure 3a). To certify this result, artificial thrombosis model produced by thrombin and vein blood was further established. The absorbance of the supernatant was examined at 450 and 540 nm as indicators of fibrin and hemoglobin. After incubation with RGD-PMCS and irradiation with an 808 nm laser, the photothermal and photodynamic ablation process of the clot was monitored. And the fibrin absorption curve was prominently increased after 4 min irradiation, suggesting the synergistic effect of PTT/PDT on thrombus with subsequent disintegration (Figure 3b,c). Additionally, the hydrodynamic size of the released fragments after the treatment revealed by DLS was $\approx 1.1 \mu\text{m}$, which could be eventually filtered through the anticlogging system of glomerular filtration membranes to avoid embolism in the cardiovascular system (Figure S6, Supporting Information).^[19] Considering that the erythrocytes are the constituent parts of the thrombus, their apoptosis is indispensable for clot thorough

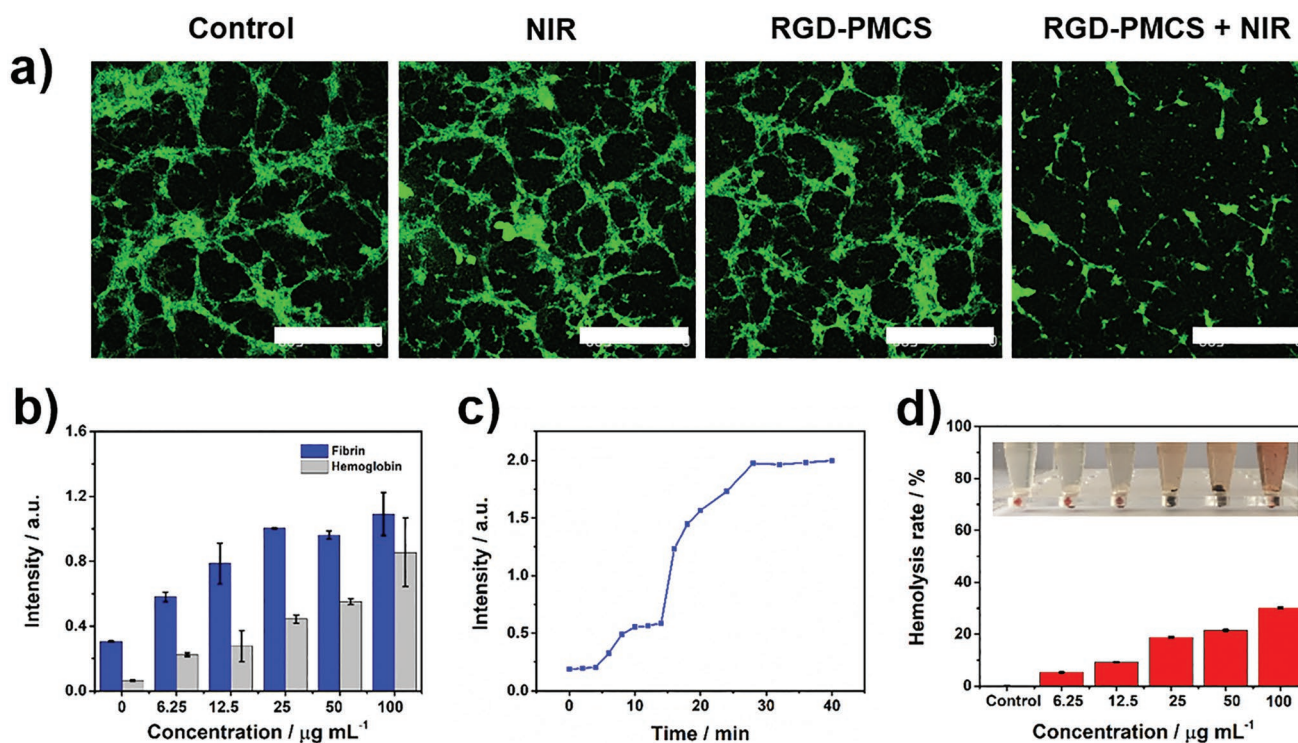


Figure 3. a) Confocal laser scanning microscopy (CLSM) images of fibrin clots after incubation with 100 $\mu\text{g mL}^{-1}$ RGD-PMCS with or without NIR laser irradiation (808 nm, 2 W cm^{-2} , 3 min). Scale bar = 500 μm . b) Level of fibrin and hemoglobin in artificial blood clot supernatant incubated with various concentrations of RGD-PMCS and irradiated by an 808 nm laser (2 W cm^{-2} , 20 min). c) Fibrin levels in artificial blood clot supernatant after treatment with RGD-PMCS (100 $\mu\text{g mL}^{-1}$) and NIR laser (808 nm, 2 W cm^{-2}) at different time points. d) Hemolysis rate of RGD-PMCS at different concentrations after irradiated by an 808 nm laser (2 W cm^{-2} , 3 min). The inset shows the corresponding photograph of hemolysis. The group irradiated by the laser without RGD-PMCS was adopted as a control.

disintegration. So hemolysis analysis induced by PTT/PDT of RGD-PMCS was performed. As shown in Figure 3d, the hemolysis rate of erythrocytes dramatically boosted with the increasing RGD-PMCS and 100 $\mu\text{g mL}^{-1}$ RGD-PMCS solution resulted in 30% cells ruptured under 808 nm laser irradiation. This result was additionally certified with the help of calcein-AM, a fluorescent probe for indicating living cells. Erythrocytes in NIR and RGD-PMCS groups showed high viability, and no apparent apoptosis was discerned. By comparison, when combined NIR laser with nanomaterials, the intracellular fluorescence signal decreased rapidly, illustrating the effective erythrocytes killing ability of RGD-PMCS (Figure S7, Supporting Information).

Thrombus-specific targeting strategy of RGD-PMCS was based on the expressed GPIIb/IIIa receptors on activated platelets (Figure 4a). In the initial platelets aggregation process, the multiple adhesive ligands, such as von Willebrand factor (VWF) and exposed collagen on damaged subendothelial matrix, bind the integrins on activated platelets, including GPIb-IX-V and GPVI receptors. Besides, the subsequent propagation of thrombi is driven by agonists released from the platelets, including ADP and thromboxane A2 (TXA2). And the fibrinogens combine the activated GPIIb/IIIa receptors to cross-link the activated platelets, which increase the density of the thrombus.^[20] Herein, RGD-PMCS could competitively combine the activated GPIIb/IIIa receptors to avoid further

thrombus formation. To quantitatively evaluate the targeting capabilities of the designed nanoparticles, inductively coupled plasma mass spectrometry was used to detect the Zn concentration on activated platelets after co-culturing with PMCS and RGD-PMCS. Compared with the PMCS group, a significant higher quantify of Zn (4.2 $\mu\text{g mL}^{-1}$) was detected in the RGD-conjugated particles, thereby allowing for greater in vivo targeting therapy (Figure S8, Supporting Information). Carbon-based nanoparticles have been investigated as photoacoustic (PA) contrast agents with high tissue penetration and excellent spatial resolution due to high NIR absorption. Here, we identified the PA signals of PMCS and RGD-PMCS in lower limb thrombus model to evaluate the specific target ability of RGD. On account of the effective RGD-PMCS accumulation at the thrombotic site, the signals especially reached a maximum at 1 h post intravenous injection, approximately 5 h faster than that of PMCS, demonstrating its great potential to effectively shorten the treatment time for thrombolysis (Figure S9, Supporting Information). Subsequently, inspired by the positive synergistic effects of RGD-PMCS-mediated PDT/PTT in vitro, we further verified the in vivo therapeutic effects for lower limb blood vessel of rats. First, the changes of local temperature at the thrombotic site under NIR light irradiation were monitored by an infrared thermal imager. It was found that the thrombotic temperature in phosphate buffered saline (PBS) injection group and PMCS + NIR group

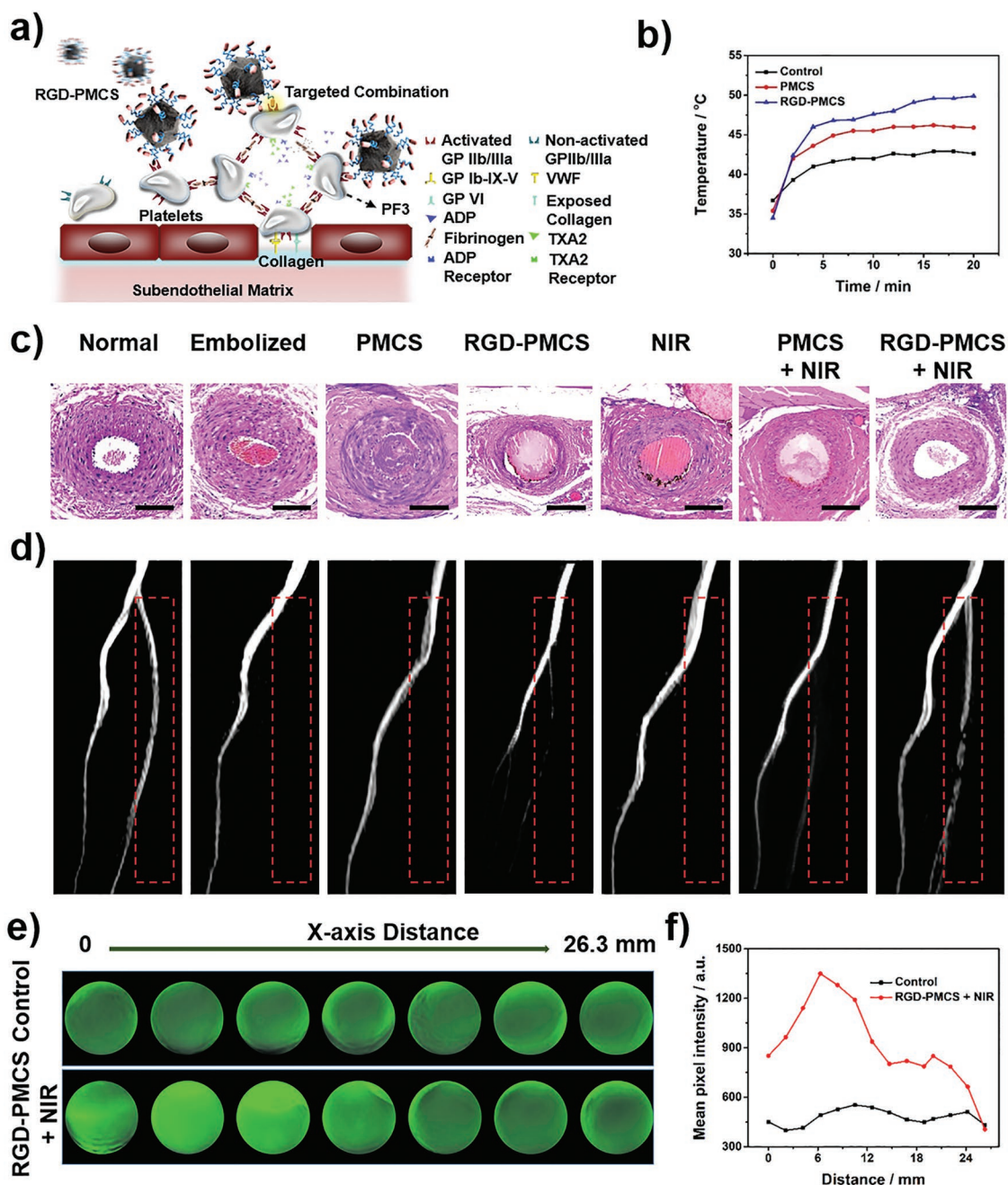


Figure 4. a) Scheme for site-specific targeting thrombus of RGD-PMCS. b) Temperature increase curves of left lower limb of rats intravenously injected with PBS, PMCS (10 mg kg^{-1}), and RGD-PMCS (10 mg kg^{-1}) and irradiated by NIR laser (2 W cm^{-2} , 20 min). c) Histopathology and d) MRI of rats after various treatments. Scale bar = $100 \mu\text{m}$. The red dashed line indicates the site of thrombus. e) PA images and f) Quantitative analysis of the signals collected from simulated blood vessel in different cross sections after different treatments (2 W cm^{-2} , 10 min).

increased about 5.9 and $10.5 \text{ }^\circ\text{C}$, respectively, while the temperature treated with RGD-PMCS under 808 nm laser irradiation increased about $14.6 \text{ }^\circ\text{C}$, confirming effective accumulation of RGD-PMCS and the possibility of *in vivo* thrombus destruction via the local hyperthermia (Figure 4b, and Figure S10, Supporting Information). For discovering the therapeutic effects *in vivo*, the rats were randomly divided into seven groups: 1) normal group; 2) embolized group; 3) PMCS group; 4) RGD-PMCS group; 5) NIR group; 6) PMCS + NIR group;

7) RGD-PMCS + NIR group. Histopathology assessments showed that nearly no thrombus in the blood vessels in the RGD-PMCS + NIR group after the one-time treatment (Figure 4c). Additionally, magnetic resonance imaging (MRI) verified the embolism and recanalization of the treated vessels (Figure 4d). The regional blood signal intensity of the RGD-PMCS + NIR group was 2.7-fold and 7.7-fold than that of the PMCS + NIR group

and RGD-PMCS group, and achieving relatively high thrombolytic effect with re-establishment ratio up to 87.9% compared with the normal blood vessels (Figure S11, Supporting Information).

The mice treated with PMCS and RGD-PMCS showed there was no obvious body weight loss during the observation period (Figure S12, Supporting Information). And no side effect was detected in major tissue slices, indicating that negligible toxicity of the treatment group, which was consistent with the hematology analysis (Figure 2c, and Figure S13, Supporting Information). To analyze the biodistribution of nanoparticles in vivo, healthy BALB/c mice were injected with fluorescent dye indocyanine green-conjugated RGD-PMCS. The results showed that accompanied with the extension of the nanoparticles circulation time, the fluorescence signal of major organs gradually decreased, indicating part of particles could be metabolized from the body (Figure S14, Supporting Information).

Anticoagulant ability of PDT induced by PF3 peroxidation damage was further evaluated via the mouse tail tip transection model, which has been extensively used to analyze the anticoagulant effect of mice that administrated with antiplatelet drugs. Mice treated with RGD-PMCS + NIR showed 2.4-fold and 1.5-fold longer bleeding time compared with the control group and PMCS + NIR group, proving the anticoagulant potential of PDT (Figure S15, Supporting Information).

Research on PTT has shown that thermal energy could increase the tissue penetration of nanomaterials.^[21] So we assumed that the energy could also promote RGD-PMCS into the deeper site of thrombus via local photothermal effect. To evaluate the penetration efficacy of RGD-PMCS cooperated with NIR laser irradiation, the simulated blood vessel was established. And the PA imaging was used to observe the position of the contrast agents. As illustrated in Figure 4e,f, the clot of the synergistic group displayed a crucial signal enhancement with a penetration of about 26.3 mm, suggesting the designed PTT/PDT synergistic therapy could not only remove the thrombus and produce a specific antiplatelet effect by hyperthermia and ROS, but also enhanced the penetration of the nanomaterials.

In summary, we have demonstrated the resultant RGD-PMCS exhibited satisfactory thrombus-targeting ability to the GPIIb/IIIa receptors on activated platelets at thrombus sites. With the enhanced accumulation of RGD-PMCS and shortened therapeutic time, the dual-modality PTT/PDT systematic therapy mediated by RGD-PMCS could be efficiently utilized for thrombolysis without secondary embolism. In addition, PDT-induced high-efficiency ROS could damage the PF3 by lipid peroxidation, thereby avoiding re-embolism. Overall, the great biosafety and effectiveness suggest that this dual-modality therapeutic strategy holds a promising future for thrombus therapy.

Experimental Section

Experimental details and additional characterization can be found in the Supporting Information. All the experiments and animal procedures were conducted in accordance with the Guidelines of the Animal

Experiments and Experimental Animals Management Committee of Capital Medical University. The study protocol was approved by the Animal Experiments and Experimental Animal Welfare Committee of Capital Medical University (Permit Number: AEEI-2017-117).

Supporting Information

Supporting Information is available from the Wiley Online Library or from the author.

Acknowledgements

F.R.Z. and Y.H.L. contributed equally to this work. This work was financially supported by National Natural Science Foundation of China (Nos. 21822802, 91749127, 81830056, 51772018, and 51572271), the National Key Research and Development Program of China (2016YFA0201500), the Fundamental Research Funds for the Central Universities (buctrc201915, PYBZ1825, and XK1802-8), and Beijing Natural Science Foundation (Nos. 17L20253 and 7191003).

Conflict of Interest

The authors declare no conflict of interest.

Keywords

carbon nanostructures, photodynamic therapy, photothermal therapy, thrombus

Received: June 5, 2019

Published online:

- [1] a) GBD 2016 Stroke Collaborators, *Lancet Neurol.* **2019**, *18*, 439; b) GBD 2017 Disease and Injury Incidence and Prevalence Collaborators, *Lancet* **2018**, *392*, 1789; c) E. A. Secemsky, K. Rosenfield, K. F. Kennedy, M. Jaff, R. W. Yeh, *J. Am. Heart Assoc.* **2018**, *7*, e009047.
- [2] W. J. Powers, A. A. Rabinstein, T. Ackerson, O. M. Adeoye, N. C. Bambakidis, K. Becker, J. Biller, M. Brown, B. M. Demaerschalk, B. Hoh, E. C. Jauch, C. S. Kidwell, T. M. Leslie-Mazwi, B. Ovbiagele, P. A. Scott, K. N. Sheth, A. M. Southerland, D. V. Summers, D. L. Tirschwell, on behalf of the American Heart Association Stroke Council, *Stroke* **2018**, *49*, e46.
- [3] a) J. J. McNeil, R. Wolfe, R. L. Woods, A. M. Tonkin, G. A. Donnan, M. R. Nelson, C. M. Reid, J. E. Lockery, B. Kirpach, E. Storey, R. C. Shah, J. D. Williamson, K. L. Margolis, M. E. Ernst, W. P. Abhayaratna, N. Stocks, S. M. Fitzgerald, S. G. Orchard, R. E. Trevaks, L. J. Beilin, C. I. Johnston, J. Ryan, B. Radziszewska, M. Jelinek, M. Malik, C. B. Eaton, D. Brauer, G. Cloud, E. M. Wood, S. E. Mahady, S. Satterfield, R. Grimm, A. M. Murray, ASPREE Investigator Group, *N. Engl. J. Med.* **2018**, *379*, 1509; b) D. Strbian, P. Michel, D. J. Seiffge, J. L. Saver, H. Numminen, A. Meretoja, K. Murao, B. Weder, N. Forss, A.-K. Parkkila, A. Eskandari, C. Cordonnier, S. M. Davis, S. T. Engelter, T. Tatlisumak, *Stroke* **2014**, *45*, 752; c) S. M. Zinkstok, Y. B. Roos, on behalf of the ARTIS investigators, *Lancet* **2012**, *380*, 731.

- [4] S. K. Ghosh, T. Pal, *Chem. Rev.* **2007**, *107*, 4797.
- [5] N. Singh, A. Varma, A. Verma, B. N. Maurya, D. Dash, *Nano Res.* **2016**, *9*, 2327.
- [6] J. Shao, M. Abdelghani, G. Shen, S. Cao, D. S. Williams, J. C. M. van Hest, *ACS Nano* **2018**, *12*, 4877.
- [7] Y. Yang, W. Zhu, Z. Dong, Y. Chao, L. Xu, M. Chen, Z. Liu, *Adv. Mater.* **2017**, *29*, 1703588.
- [8] J. M. Walker, J. M. Zaleski, *Chem. Mater.* **2014**, *26*, 5120.
- [9] a) S. Ye, J. Rao, S. Qiu, J. Zhao, H. He, Z. Yan, T. Yang, Y. Deng, H. Ke, H. Yang, Y. Zhao, Z. Guo, H. Chen, *Adv. Mater.* **2018**, *30*, 1801216; b) X. Tan, S. Luo, L. Long, Y. Wang, D. Wang, S. Fang, Q. Ouyang, Y. Su, T. Cheng, C. Shi, *Adv. Mater.* **2017**, *29*, 1704196; c) P. Vijayaraghavan, C.-H. Liu, R. Vankayala, C.-S. Chiang, K. C. Hwang, *Adv. Mater.* **2014**, *26*, 6689.
- [10] a) Y. Chen, L. A. Ju, F. Zhou, J. Liao, L. Xue, Q. P. Su, D. Jin, Y. Yuan, H. Lu, S. P. Jackson, C. Zhu, *Nat. Mater.* **2019**, *18*, 760; b) B. S. Coller, S. J. Shattil, *Blood* **2008**, *112*, 3011.
- [11] C. Cui, Z. Yang, X. Hu, J. Wu, K. Shou, H. Ma, C. Jian, Y. Zhao, B. Qi, X. Hu, A. Yu, Q. Fan, *ACS Nano* **2017**, *11*, 3298.
- [12] P. E. J. van der Meijden, J. W. M. Heemskerk, *Nat. Rev. Cardiol.* **2019**, *16*, 166.
- [13] a) X. Pan, L. Bai, H. Wang, Q. Wu, H. Wang, S. Liu, B. Xu, X. Shi, H. Liu, *Adv. Mater.* **2018**, *30*, 1800180; b) S. Wang, L. Shang, L. Li, Y. Yu, C. Chi, K. Wang, J. Zhang, R. Shi, H. Shen, G. I. N. Waterhouse, S. Liu, J. Tian, T. Zhang, H. Liu, *Adv. Mater.* **2016**, *28*, 8379.
- [14] N. Kotagiri, G. P. Sudlow, W. J. Akers, S. Achilefu, *Nat. Nanotechnol.* **2015**, *10*, 370.
- [15] a) Y. Cheng, Y. Chang, Y. Feng, H. Jian, Z. Tang, H. Zhang, *Angew. Chem., Int. Ed.* **2018**, *57*, 246; b) H. Lin, Y. Wang, S. Gao, Y. Chen, J. Shi, *Adv. Mater.* **2018**, *30*, 1703284.
- [16] B. Furie, B. C. Furie, *N. Engl. J. Med.* **2008**, *359*, 938.
- [17] S. J. Montague, R. K. Andrews, E. E. Gardiner, *Blood* **2018**, *132*, 2535.
- [18] a) V. E. Kagan, G. Mao, F. Qu, J. P. F. Angeli, S. Doll, C. S. Croix, H. H. Dar, B. Liu, V. A. Tyurin, V. B. Ritov, A. A. Kapralov, A. A. Amoscato, J. Jiang, T. Anthonymuthu, D. Mohammadyani, Q. Yang, B. Proneth, J. Klein-Seetharaman, S. Watkins, I. Bahar, J. Greenberger, R. K. Mallampalli, B. R. Stockwell, Y. Y. Tyurina, M. Conrad, H. Bayır, *Nat. Chem. Biol.* **2017**, *13*, 81; b) A. Ayala, M. F. Muñoz, S. Argüelles, *Oxid. Med. Cell. Longevity* **2014**, *2014*, 1.
- [19] M. J. Moeller, V. Tenten, *Nat. Rev. Nephrol.* **2013**, *9*, 266.
- [20] S. P. Jackson, *Blood* **2007**, *109*, 5087.
- [21] a) F. Zhang, X. Han, Y. Hu, S. Wang, S. Liu, X. Pan, H. Wang, J. Ma, W. Wang, S. Li, Q. Wu, H. Shen, X. Yu, Q. Yuan, H. Liu, *Adv. Sci.* **2019**, *6*, 1801507; b) R. Zhao, X. Han, Y. Li, H. Wang, T. Ji, Y. Zhao, G. Nie, *ACS Nano* **2017**, *11*, 8103; c) J. Wang, J. Liu, Y. Liu, L. Wang, M. Cao, Y. Ji, X. Wu, Y. Xu, B. Bai, Q. Miao, C. Chen, Y. Zhao, *Adv. Mater.* **2016**, *28*, 8950.



Supporting Information

for *Adv. Sci.*, DOI: 10.1002/advs.201901378

**Metal–Organic-Framework-Derived Carbon Nanostructures
for Site-Specific Dual-Modality Photothermal/Photodynamic
Thrombus Therapy**

*Fengrong Zhang, Yuehong Liu, Jiani Lei, Shunhao Wang,
Xunming Ji, Huiyu Liu,* and Qi Yang**

Copyright WILEY-VCH Verlag GmbH & Co. KGaA, 69469 Weinheim, Germany, 2019.

Supporting Information

Metal–Organic-Framework-Derived Carbon Nanostructures for Site-Specific Dual-Modality Photothermal/Photodynamic Thrombus Therapy

Fengrong Zhang, Yuehong Liu, Jiani Lei, Shunhao Wang, Xunming Ji, Huiyu Liu, and Qi Yang**

Experimental Section

Materials. Zinc nitrate hexahydrate ($\text{Zn}(\text{NO}_3)_2 \cdot 6\text{H}_2\text{O}$), cetyltrimethylammonium bromide (CTAB), tetraethyl orthosilicate (TEOS), calcium chloride (CaCl_2), and 2-methylimidazole were obtained from Macklin Biochemical Technology Co., Ltd. (Shanghai, China). Vitamin E-polyethylene glycol-COOH (VE-PEG-COOH, MW = 5000) was purchased from Shanghai Ponsure Biotech, Inc. (Shanghai, China). Indocyanine green (ICG) and sodium citrate were purchased from Sigma, St. Louis (MO, USA). N-hydroxysuccinimide (NHS) and 1-ethyl-3(3-dimethylaminopropyl) carbodiimide hydrochloride (EDC) were purchased from Adamas-beta Corporation (Shanghai, China). Arg-Gly-Asp (RGD) motifs were obtained from GL Bio-chem Ltd. (Shanghai, China). Fluorescein isothiocyanate (FITC)-CD41 (FITC-CD41) was purchased from Biolegend (CA, USA). FITC-conjugated fibrinogen was purchased from Abcam (MA, UK). Adenosine diphosphate (ADP), 3-(4,5-Dimethylthiazol-2-yl)-2,5-diphenyltetrazolium bromide (MTT), bicinchoninic acid (BCA) assay kit, calcein acetoxymethyl ester (calcein-AM), and 2,7-dichlorodihydrofluorescein diacetate (DCFH-DA) were obtained from Beijing

Solarbio Science & Technology Co., Ltd. (Beijing, China). Rat platelet factor 3 (PF3) enzyme-linked immunosorbent assay (ELISA) kits were purchased from j&l Biological Industrial Co., Ltd. (Shanghai, China). Hematoxylin and eosin (H&E) were obtained from Boster Biological Technology Co., Ltd. (Wuhan, China). Deionized water was obtained from a Milli-Q synthesis system. All chemicals were used as received without further treatment.

Nanoparticle Characterization. A HT-7700 transmission electron microscope (TEM) was used to characterize the morphology and structure of metal–organic framework–derived mesoporous carbon nanospheres containing porphyrin-like metal centers (PMCS). Element mapping and energy-dispersive X-ray spectroscopy (EDS) spectrum of PMCS and RGD motifs modified PMCS (RGD-PMCS) were performed by APOLLO XLT2 TEM. Zeta potentials and the hydrodynamic size of PMCS and RGD-PMCS were analyzed by Zetasizer Nano-ZS (Malvern Instruments, UK). Fourier transform infrared spectra were acquired with a Nicolet 6700 spectrometer by using the KBr pellet method. The ultraviolet-visible-infrared absorption spectrum was obtained by 2600 UV-visible Spectrophotometer (SHIMADZU, Japan). An infrared thermal imager (FLIR SC 620; FLIR system, Inc., Wilsonville, OR, USA) was used to record the photothermal images. And the temperature was acquired with a thermocouple (TES 1315, TES Electrical Electronic Corp., Taiwan, China). Porphyrin-like structure in the PMCS was analyzed by ESCALab220i-XL high-performance electron spectrometer. Singlet oxygen ($^1\text{O}_2$) production was quantified by using Bruker ELEXSYS E500 CW electron spin resonance (ESR)

spectrometer.

Preparation of PMCS. PMCS were prepared by carbonization of an imidazolate framework according to our earlier reports.^[1,2] Firstly, 33.75 mmol 2-methylimidazole dissolved in 100 mL methanol was poured into a solution containing 8 mmol $\text{Zn}(\text{NO}_3)_2 \cdot 6\text{H}_2\text{O}$ in (100 mL), and then stirred at room temperature for 3 h. The obtained zeolitic-imidazolate-framework (ZIF-8) nanoparticles were collected by centrifugation and washed three times with methanol. Later, ZIF-8 nanoparticles were dispersed in 240 mL 10 vol% methanol, and the mixture was adjusted to pH 11 by NaOH aqueous, and 0.2 g CTAB was further added. After stirring at 500 rpm for 30 min, 1.2 mL TEOS was added into the above solution, followed by stirring for another 30 min. The obtained ZIF-8 core/mesoporous silica shell (ZIF-8@mSiO₂) nanoparticles collected by centrifugation and washed three times with ethanol and then dried at 60 °C. Next, the prepared ZIF-8@mSiO₂ nanoparticles were pyrolyzed at 800 °C for 2 h with the help of flowing N₂, and then cooled to room temperature. Then, the pyrolyzed sample was etched by 4 M NaOH solution at 80 °C for 3 h. The final product was collected by centrifugation and washed several times with ultrapure water until the value of pH was close to neutral.

Preparation of RGD-PMCS. Firstly, 2 mg PMCS were mixed with 2 mg VE-PEG-COOH in 3 mL of ultrapure water. After vibrating at 37 °C for 4 h, the precipitates were washed three times with deionized water and collected after 10-min centrifugation at 12000 rpm. Then, 3 mL deionized water was supplemented, and the pH was adjusted to 6.0 with hydrochloric acid. Subsequently, 58 mM NHS (200 μL)

and 200 mM EDC (200 μ L) were added. After vibrating for 1 h at 37 $^{\circ}$ C, 2 mg RGD peptide was added into the mixture. After 3 h, the solution was centrifuged at 15000 rpm for 10 min and the precipitate was washed three times. The residual RGD concentration in the supernatant was measured by the BCA protein assay. The conjugation efficiency of RGD (%) = (RGD input - free RGD in the supernatant)/RGD input \times 100%. The final conjugation efficiency of RGD was 28.5%.

Preparation of ICG-Conjugated RGD-PMCS (ICG-RGD-PMCS). The prepared RGD-PMCS were resuspended in 3 mL ultrapure water and adjust the pH value to 6.0 with hydrochloric acid. Subsequently, NHS (58 mM, 200 μ L) and EDC (200 mM, 200 μ L) were added and vibrated for 1 h at 37 $^{\circ}$ C, and ICG was further added. The mixture was then vibrated at 4 $^{\circ}$ C overnight, and ICG-RGD-PMCS were obtained by centrifugation again.

In Vitro Photothermal Measurement. A series of PMCS aqueous dispersions (1 mL) with different concentrations (0, 6.25, 12.5, 25, 50, 100 μ g mL $^{-1}$) were irradiated with near-infrared (NIR) laser (2 W cm $^{-2}$) for 20 min, and the temperature change was recorded by a thermocouple and the photothermal images were acquired by an infrared thermal imager.

$^1\text{O}_2$ Measurements by ESR. Production of $^1\text{O}_2$ by PMCS (100 μ g mL $^{-1}$) with or without NIR irradiation (808 nm, 2 W cm $^{-2}$, 3 min) was evaluated by ESR spectrometer with 2,2,6,6-tetramethylpiperide (TEMP) as the trapping probe.

Platelets and Red Blood Cells Preparation. Sprague Dawley (SD) rats, male,

weighed 250-300 g, were purchased from Beijing Vital River Laboratory Animal Technology Co. Ltd and all the experiments and animal procedures were conducted in accordance with the Guidelines of the Animal Experiments and Experimental Animals Management Committee of Capital Medical University. The study protocol was approved by the Animal Experiments and Experimental Animal Welfare Committee of Capital Medical University (Permit Number: AEEI-2017-117). Blood was drawn from the inferior vein of healthy rats under anesthesia and collected in heparinized tubes with 4% sodium citrate (1 mL) to avoid coagulation. For experiments involving washed platelets, the whole blood was centrifuged at 800 rpm for 8 min. The platelet-rich plasma (PRP) in the supernatant was further diluted by 5 mL Tyrode's solution and centrifuged at 3500 rpm for 10 min and the precipitate was washed by Tyrode's solution for three times. For experiments with washed red blood cells, the whole blood was separated by centrifugation at 2000 rpm for 10 min, and then washed three times with phosphate buffered saline (PBS).

In Vitro Blood Biosafety Evaluation. To demonstrate that the photosensitizers could not activate platelets in the blood, the prepared platelets were diluted with Tyrode's solution with a density of 1×10^7 per milliliter and divided into four groups: a) Positive control group, b) Negative control group, c) NIR group (808 nm, 2 W cm^{-2} , 3 min), d) RGD-PMCS group ($100 \mu\text{g mL}^{-1}$). For the positive control group, the platelets were activated with $10 \mu\text{M}$ ADP ($250 \mu\text{L}$) at $37 \text{ }^\circ\text{C}$ for 10 min. After adding 5 mM CaCl_2 ($50 \mu\text{L}$) and $50 \mu\text{g mL}^{-1}$ FITC-CD41 ($10 \mu\text{L}$), all groups were incubated at room temperature for 1 h and evaluated via flow cytometry. For hemolysis evaluation,

the collected red blood cells were diluted to 1/10 of their volume with PBS. Then 200 μL RGD-PMCS with different concentrations were added into 1.3 mL freshly isolated blood and then kept at 37 °C for 4 h, followed by centrifugation at 3000 rpm for 10 min. After that, the supernatant was collected and measured absorbance at 540 nm. PBS was acted as the negative control and deionized water was adopted as the positive control. Hemolysis ratio was calculated by the following formula: hemolysis % = (sample absorbance – negative control absorbance)/(positive control absorbance – negative control absorbance) \times 100%.

In Vitro Cell Cytotoxicity Test. The human umbilical vein endothelial cells (HUVEC) were obtained from Peking Union Medical College Hospital (Peking, China). Fetal bovine serum (FBS), Ham's F12K, heparin, endothelial cell growth supplement (ECGS), L-glutamine, penicillin, and streptomycin were obtained from Corning (New York, USA). The cells were maintained in Ham's F12K medium with heparin (0.1 mg mL^{-1}), ECGS (0.05 mg mL^{-1}), 10% FBS, 1% L-glutamine and 1% penicillin/streptomycin at 37 °C containing 5% CO_2 . For in vitro cytotoxicity test, HUVECs were seeded into 96 well plates with a density of 1×10^4 per well. After 24 h, cells were incubated with RGD-PMCS for another 24 h. The MTT assay was conducted following the standard protocol.

In Vitro Synergistic Therapy. Red blood cells were incubated with 100 $\mu\text{g mL}^{-1}$ RGD-PMCS for 24 h. Subsequently, the cells were irradiated with an 808 nm laser at a power intensity of 2 W cm^{-2} for 3 min, and cultured for another 24 h. Then, the cells were stained with calcein-AM, followed by a Leica SP5 confocal laser scanning

microscope (CLSM) observation. Quantitative analysis was also taken followed the operation as the above treatments. Then the red blood cells were stained with DCFH-DA for 30 min and evaluated through a BioTek Powerwave XS fluorescence microplate reader.

For hemolysis treatment analysis, the diluted red blood cells were incubated with various concentrations of RGD-PMCS, followed by irradiating with the 808 nm laser (2 W cm^{-2}) for 3 min. After that, all operations were the same as the hemolysis evaluation described above.

Level of PF3 Detection. The prepared platelets were diluted with Tyrode's solution with a density of 1×10^{12} per milliliter and then treated with various concentrations of RGD-PMCS. After 1 h incubation, those platelets were subjected to irradiation of NIR laser (808 nm, 2 W cm^{-2} , 3 min). Then, the platelets were seeded into 96-well plates and kept at $37 \text{ }^{\circ}\text{C}$ for 30 min. Subsequently, the excess solution was removed and washed with detergent for 5 times, the platelets were incubated with enzyme standard reagent, incubated and washed in the same manner as described above. In addition, platelets were further incubated with Reagent A and then with Reagent B according to the protocol. After that, the reaction was stopped with Stop solution and measured absorbance at 540 nm.

FITC-Labeled Fibrin Clots Assay. FITC-labeled fibrin clots were induced by the addition of 25 U mL^{-1} thrombin and 2.5 mM CaCl_2 into a fibrinogen solution containing 1 mg mL^{-1} fibrinogen ($450 \text{ }\mu\text{L}$) and 1 mg mL^{-1} FITC-labeled fibrinogen ($50 \text{ }\mu\text{L}$), followed by incubation at $37 \text{ }^{\circ}\text{C}$ for 1 h. The colt was incubated with

RGD-PMCS ($100 \mu\text{g mL}^{-1}$, $500 \mu\text{L}$) for 1 h and further irradiated with 808 nm laser (2 W cm^{-2} , 3 min) and evaluated through a CLSM.

In Vitro Target Specificity. The prepared activated platelets were diluted with Tyrode's solution and incubated with $100 \mu\text{g mL}^{-1}$ PMCS and RGD-PMCS for 1 h. The platelets were then washed three times with Tyrode's solution, and $200 \mu\text{L}$ aqua regia was added, the amount of Zn was measured by inductively coupled plasma mass spectrometry (X Series 2; ThermoFisher, Waltham, MA, USA).

Artificial Thrombosis Assay. Inferior vein blood was collected from healthy rats under anesthesia. Artificial thrombosis was produced by adding 25 U mL^{-1} thrombin and 25 mM CaCl_2 at $37 \text{ }^\circ\text{C}$ for 3 h. The resulted clot was incubated with different concentrations of RGD-PMCS for 1h and further exposed to 808 nm irradiation for 20 min at a power density of 2 W cm^{-2} , the absorbance at 540 nm and 340 nm were monitored. In addition, the hydrodynamic size of the artificial thrombosis supernatant was monitored at 10-min intervals by dynamic light scattering.

Lower Limb Thrombosis Model. SD rats (male, weighted 250-300 g) were anesthetized with chloral hydrate. For each of rat, the left lower limb was fixed after the pre-operation skin preparation, and then an incision was made to expose the targeting lower limb artery. One piece of filter paper saturated with 10% FeCl_3 was placed on the top of the left lower limb artery for 10 min to generate vascular injury. As for the mice (BALB/c, male, aged 6-8 weeks) thrombosis model, the lower limb artery was dealt with 5% FeCl_3 for 10 min.

In Vivo PA Imaging. The mice with lower limb thrombosis were intravenously

injected with PMCS (10 mg kg⁻¹) and RGD-PMCS (10 mg kg⁻¹), respectively, and photoacoustic (PA) images were collected by real-time multispectral optoacoustic tomography (MSOT inVision 128, iThera medical, Germany).

In Vivo Infrared Thermal Imaging. The rats with lower limb thrombosis were intravenously injected with PBS, PMCS (10 mg kg⁻¹) and RGD-PMCS (10 mg kg⁻¹), respectively. The thrombotic site was irradiated by NIR light (2 W cm⁻²) for 20 min after 1 h post-injection, and the changes of temperature at the thrombotic site were monitored by an infrared thermal imager.

In Vivo Thrombosis Therapy. The rats with thrombosis were randomly divided into seven groups: 1) Normal group; 2) Embolized group; 3) PMCS group (10 mg kg⁻¹); 4) RGD-PMCS group (10 mg kg⁻¹); 5) NIR group (2 W cm⁻², 20 min); 6) PMCS + NIR group (10 mg kg⁻¹, 2 W cm⁻², 20 min); 7) RGD-PMCS + NIR group (10 mg kg⁻¹, 2 W cm⁻², 20 min). All of the treatments carried out only once. The H&E of major organs (heart, liver, spleen, lung, and kidney) and blood vessels were performed 1 day after treatments to assess the biosafety and thrombolytic effect of RGD-PMCS. Body weights of mice were recorded every three days.

Magnetic Resonance Imaging. During the Magnetic Resonance Imaging (MRI) scanning, rats in each group were continually sedated by chloral hydrate. All images were obtained from a 7-Tesla MRI scanner (Bruker, Germany). The experimental groups were shortly imaged after thrombus induction with the body coil of rats (Bruker, Germany).

After the scanning of the localizer, a 2-dimensional, time-of-flight magnetic

resonance angiogram was performed from the level of iliac bifurcation to the terminal lower limbs blood vessels. Sequence parameters were as follows: repetition time/echo time = 18/4.5 ms, number of averages = 3, and excitation pulse angle = 76°. With a 256 × 256 matrix, a field of view of 55 × 55 mm was scanned with 100 continuous slices of 600 μm thickness. In addition, the saturated zone was used to reduce the impacts of breath and lightly move to image quality. We also took some measures to protect rats from damages of low body temperature before and after scanning. The total scanning time was about 18 min.

The post-processed angiographic images, including 3-dimensional reconstructed images with the maximum-intensity project algorithm were made by Horos (version 3.3.5). The lower limb blood vessels of various groups were equally divided into three segments. Then, the quantitative analysis was provided in each segment by calculating the MRI signal area ratio, which was defined in accordance with the following equation: (Signal Area of Experimental Blood Vessel/Signal Area of Normal Blood Vessel) × 100%.

In Vivo Biodistribution. The healthy mice were injected via the tail with ICG-RGD-PMCS (10 mg kg⁻¹) (three mice per group). Then, the mice were sacrificed and major organs (heart, liver, spleen, lung, and kidney) were collected at 6, 12, 24, and 48 h post-injection. The fluorescence intensity organs were measured via using an IVIS Spectrum Imaging System (PerkinElmer, Waltham, MA, USA).

Tail Bleeding Assay. The mice with thrombosis were divided randomly into seven groups with the same operations as in vivo thrombosis therapy described above. A

distal segment with 10 mm of the tail was cut by anatomical scissors and the injured tail was put into 37 °C saline. The bleeding time was defined as the time needed for a wound to hemostasis for at least 10 s.

Intra-Thrombosis Penetration Analysis. Blood collected from the inferior vein of healthy rats was injected into a plastic pipette and the other end was closed. Artificial thrombosis was produced by adding 25 U mL⁻¹ (100 µL) thrombin and 25 mM CaCl₂ at 37 °C for 3 h. The resulted clot was incubated with RGD-PMCS (1 mg mL⁻¹, 1 mL) and further exposed to 808 nm irradiation for 10 min at a power density of 2 W cm⁻², the PA signals pre- and post-treatment with RGD-PMCS were recorded by MSOT.

Statistical Analysis. All data were presented as the mean ± standard deviation or mean. Statistical analysis was conducted by using t-test: ns: $P > 0.05$, * $P < 0.05$, ** $P < 0.01$, *** $P < 0.001$.

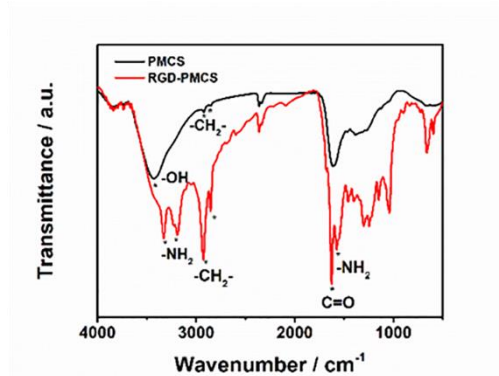


Figure S1. Fourier transform infrared spectra of PMCS and RGD-PMCS.

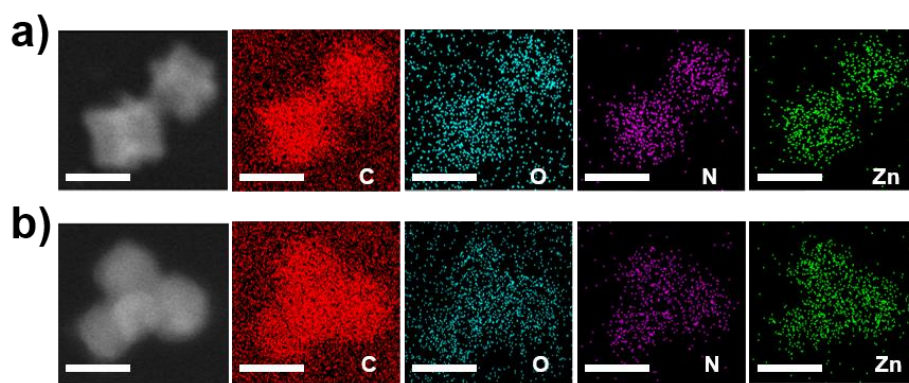


Figure S2. Elemental mapping for a) PMCS and b) RGD-PMCS. Scale bar = 100 nm.

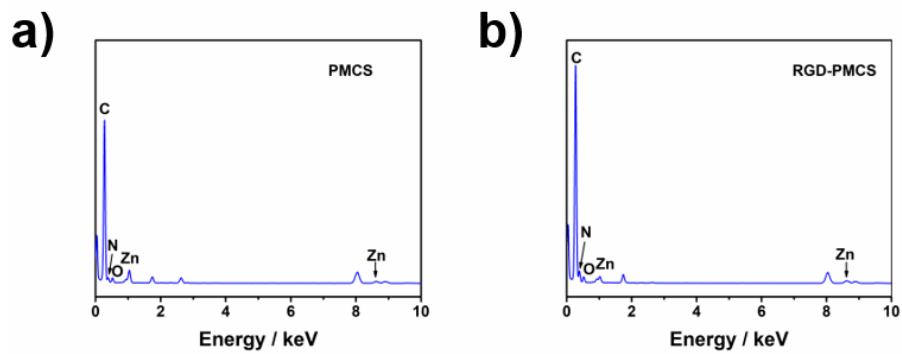


Figure S3. Energy-dispersive X-ray spectra of a) PMCS and b) RGD-PMCS.

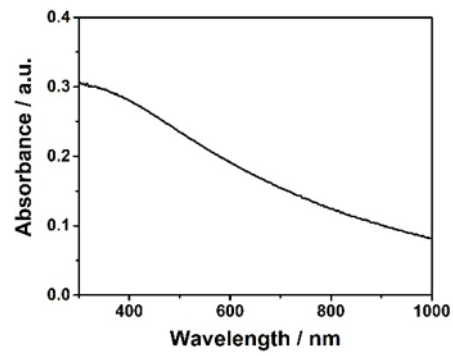


Figure S4. UV-vis-NIR absorption spectrum of PMCS.

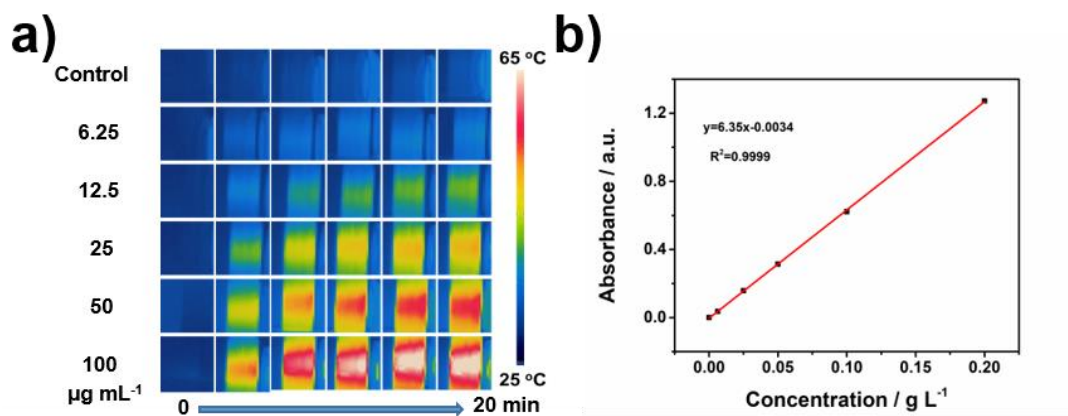


Figure S5. a) Infrared thermal images of PMCS at different concentrations under an 808 nm laser irradiation (2 W cm^{-2} , 20 min). b) Fitting curve of the absorption values at 808 nm of PMCS dispersions with different concentrations in water.

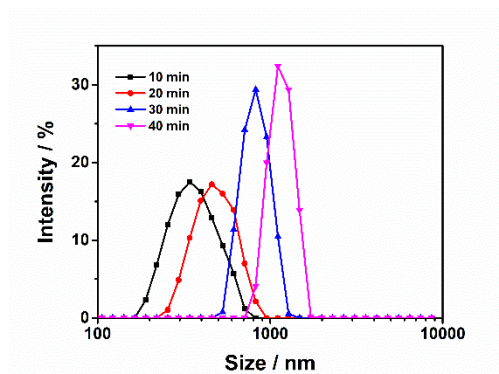


Figure S6. Hydrodynamic size of the released fragments treated with RGD-PMCS ($100 \mu\text{g mL}^{-1}$) and NIR laser (808 nm , 2 W cm^{-2}) at different time points.

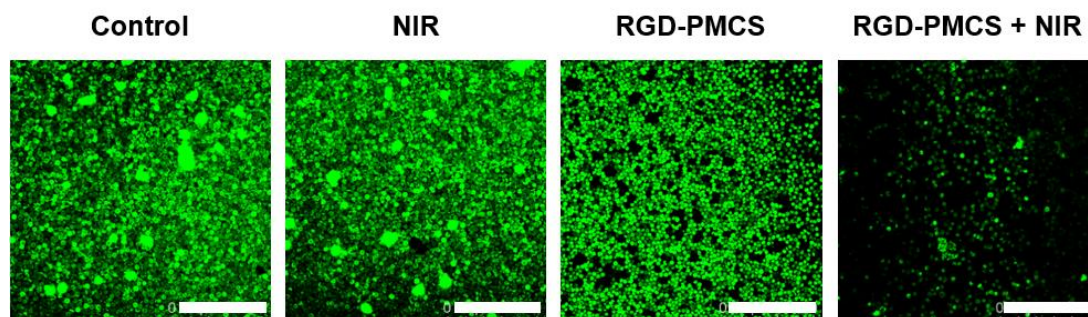


Figure S7. CLSM images of red blood cells stained with calcein-AM after co-incubating with RGD-PMCS ($100 \mu\text{g mL}^{-1}$) and irradiating with NIR laser (808 nm , 2 W cm^{-2} , 3 min). Scale bar = $100 \mu\text{m}$.

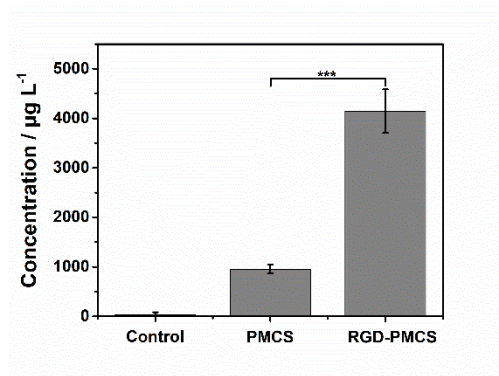


Figure S8. Quantitative analysis of Zn concentration in platelets after incubation with PMCS and RGD-PMCS. $P > 0.05$, $*P < 0.05$, $**P < 0.01$, $***P < 0.001$.

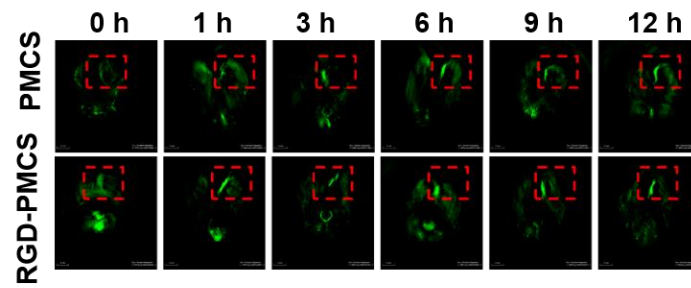


Figure S9. PA imaging of mice after intravenous injection of PMCS (10 mg kg^{-1}) and RGD-PMCS (10 mg kg^{-1}).

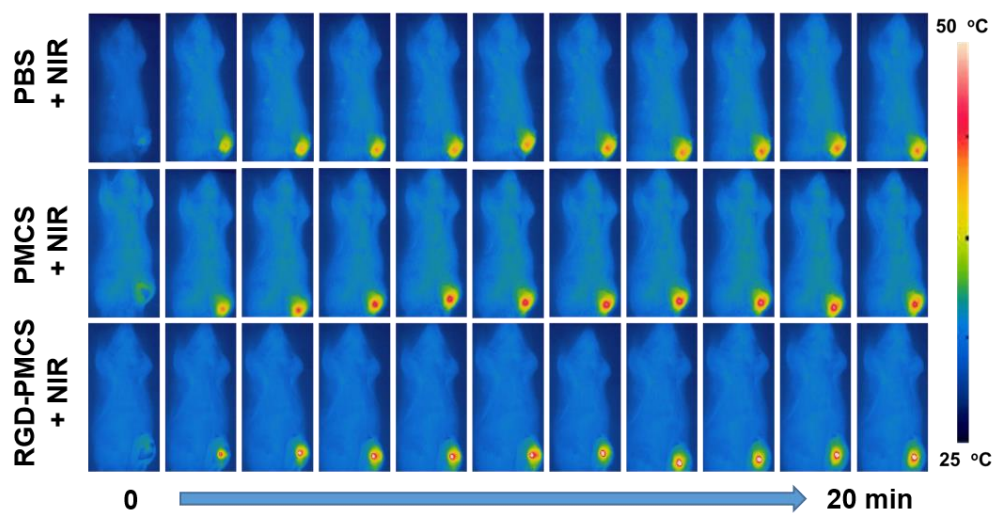


Figure S10. Infrared thermal images of rats intravenously injected with PBS, PMCS (10 mg kg^{-1}), and RGD-PMCS (10 mg kg^{-1}) and irradiated with NIR laser (2 W cm^{-2} , 20 min).

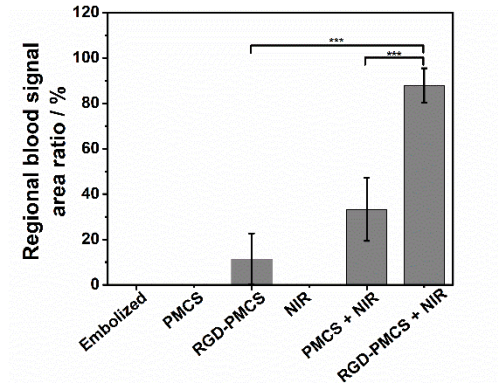


Figure S11. Quantitative analysis of MRI signal area ratio between the thrombotic vessels after various treatments and normal blood vessels. $P > 0.05$, $*P < 0.05$, $**P < 0.01$, $***P < 0.001$.

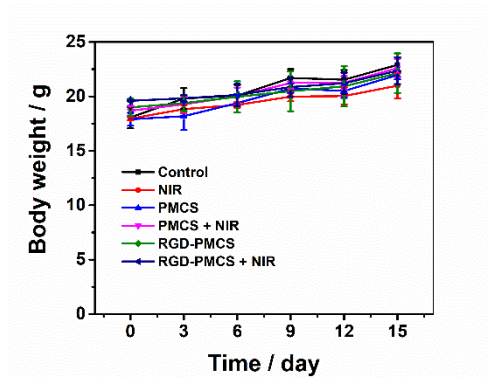


Figure S12. Body weights of variation of mice in different groups after various treatments.

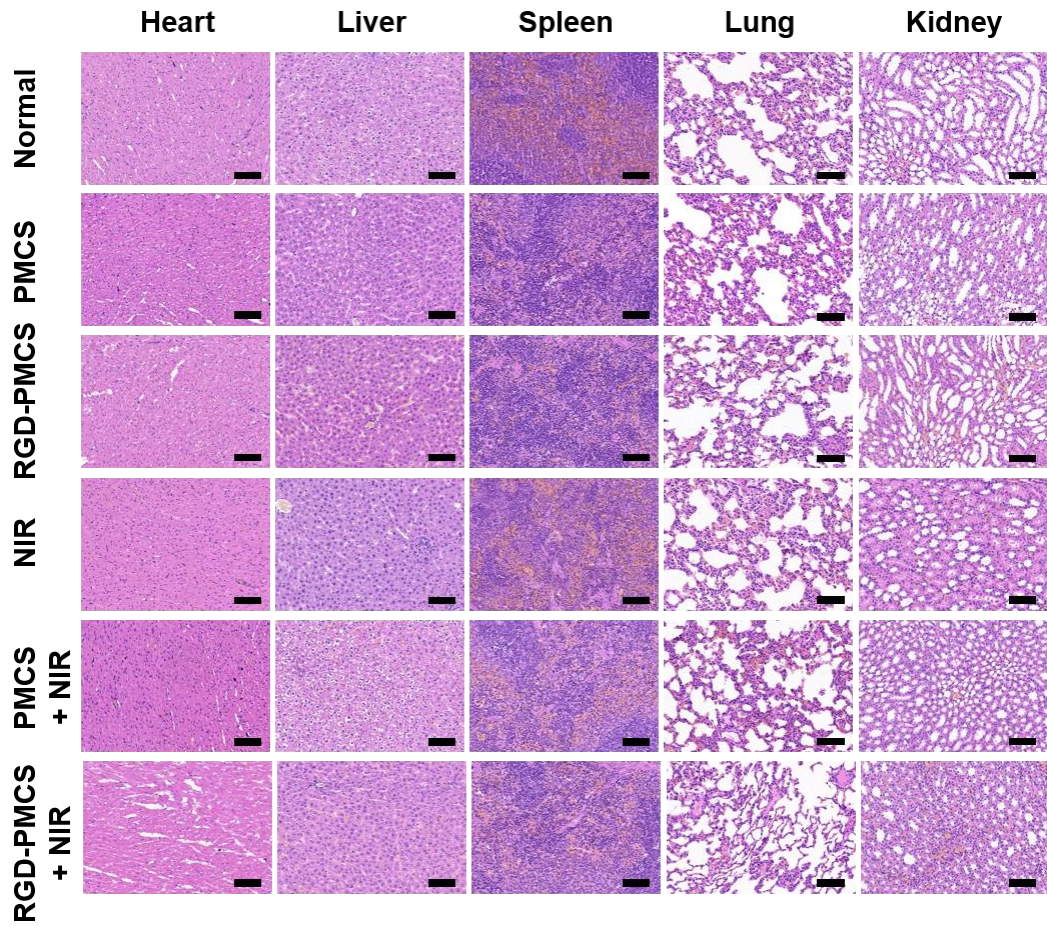


Figure S13. H&E stained images of major organs after various treatments. Scale bar = 100 μ m.

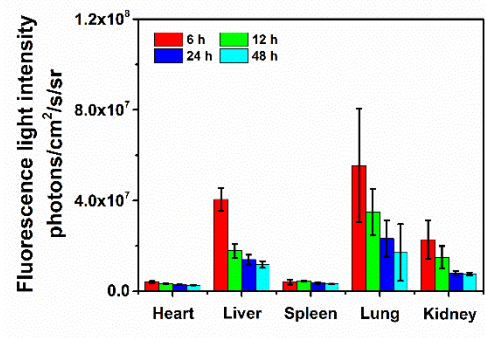


Figure S14. Quantitative analysis of fluorescence in major organs collected from mice with RGD-PMCS injection at different time points.

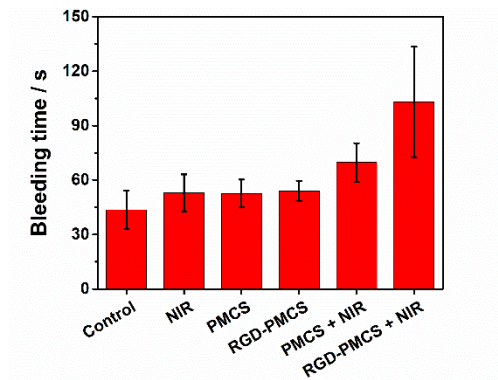


Figure S15. Bleeding time of the mice transected tail with different treatments.

References

- [1] X. Pan, L. Bai, H. Wang, Q. Wu, H. Wang, S. Liu, B. Xu, X. Shi, H. Liu, *Adv. Mater.* **2018**, *30*, 1800180.
- [2] S. Wang, L. Shang, L. Li, Y. Yu, C. Chi, K. Wang, J. Zhang, R. Shi, H. Shen, G. I. N. Waterhouse, S. Liu, J. Tian, T. Zhang, H. Liu, *Adv. Mater.* **2016**, *28*, 8379.